hydrogen

MDPI

Article

Hydrogen-Induced Intergranular Fracture Behavior Accelerated by Needle-like MC Carbide in IN740H Superalloy

Seung-Yong Lee [1], Han-Jin Kim [1], Chang-Ho Ahn [2], Seung-Wook Baek [2], Jae-Hyeok Shim [1] and Jin-Yoo Suh [1,*]

[1] Center for Energy Materials Research, Korea Institute of Science and Technology (KIST), Seoul 02792, Republic of Korea
[2] Interdisciplinary Materials Measurement Institute, Korea Research Institute of Standards and Science (KRISS), 267 Gajeongro, Yuseong-Gu, Daejeon 34113, Republic of Korea
* Correspondence: jinyoo@kist.re.kr

Abstract: Hydrogen embrittlement of a Ni-based superalloy, IN740H, was evaluated after gas-phase hydrogen pre-charging. Specimens with different grain sizes were prepared to induce different precipitation behavior under annealing treatment; the formation of needle-like MC carbide was found only in a specimen with a larger grain size and incoherent twin boundaries after annealing treatment at 1173 K. While other parameters including the grain size and annealing treatment turned out not to undermine the resistance to hydrogen embrittlement, the needle-like MC carbide was found to induce premature failure after hydrogen absorption.

Keywords: Ni-based superalloy; hydrogen embrittlement; tensile property; incoherent twin boundary; carbide morphology

check for updates

Citation: Lee, S.-Y.; Kim, H.-J.; Ahn, C.-H.; Baek, S.-W.; Shim, J.-H.; Suh, J.-Y. Hydrogen-Induced Intergranular Fracture Behavior Accelerated by Needle-like MC Carbide in IN740H Superalloy. *Hydrogen* **2022**, *3*, 474–487. https://doi.org/10.3390/hydrogen3040030

Academic Editor: George E. Marnellos

Received: 21 October 2022
Accepted: 21 November 2022
Published: 23 November 2022

Publisher's Note: MDPI stays neutral with regard to jurisdictional claims in published maps and institutional affiliations.

Copyright: © 2022 by the authors. Licensee MDPI, Basel, Switzerland. This article is an open access article distributed under the terms and conditions of the Creative Commons Attribution (CC BY) license (https://creativecommons.org/licenses/by/4.0/).

1. Introduction

Recently, several Ni-based superalloys have received attention for their robustness in harsh conditions such as highly corrosive environment in the next generation oil and gas exploration [1–6]. Hydrogen atoms as a by-product are likely to penetrate into materials, resulting in significant mechanical degradation, which is well known as hydrogen embrittlement for wide range of engineering metals and steels [7–9]. Therefore, studies on hydrogen embrittlement (HE) of Ni-based superalloys are essential for the applicability of the alloys in such harsh conditions.

Typically, superalloys include several alloying elements, and various precipitates can form during heat-treatment as well as in-service condition. Properties of Ni-based superalloys, especially mechanical properties, vary sensitively with the precipitates, and thereby exquisite heat-treatment condition is chosen during fabricating process, in order to control the formation of the precipitates, type, size, fraction, position in microstructure, and so on. The representative precipitate of precipitation-hardened Ni-based superalloys is the gamma-prime (γ') with a $L1_2$ ordered structure, and/or gamma-double prime (γ'') with a $D0_{22}$ ordered structure. They substantially contribute to the strengthening of superalloys through the interaction between them and dislocations [10–14]. However, there have been many reports that the ordered precipitates can be detrimental to the sensitivity of hydrogen embrittlement for Ni-based superalloys [2,3]. Enhanced planar slip by shearing of the ordered precipitates tends to restrict the ability to cross-slip resulting in higher tendency for hydrogen-related failure [4–6,10,11].

Meanwhile, carbides and/or nitrides are also inevitable precipitates in most Ni-based superalloys, and they as well as the ordered precipitates form during heat-treatment of the alloys with varying stoichiometric ratio, constituent elements, crystal structure, and so on. There are different scopes reported on the effect of carbides on HE [15–19]. Araujo et al. [15] reported that the size and distribution of the (Nb,Ti)C particles can affect the degree of HE working as propagation path of hydrogen-induced crack in Inconel 718. On the other hand,

Young et al. [16] argued that grain boundary carbide precipitation is beneficial to resistance to HE in Ni-17Cr-8Fe alloys because the carbide/matrix interface acts as a strong hydrogen trap site. Commonly agreeable from those diverse results is that delicate control of the nucleation site, size, and distribution of carbides appear very important on the degree of HE of Ni-based superalloys, which makes further studies necessary to understand the effect of carbides influencing on HE of Ni-based superalloys.

Our previous study has reported that needle-like MC carbides formed at or near twin boundaries in IN740H superalloy aged at 1173 K [20]. IN740H superalloy is the state-of-the-art Ni-based superalloy, which is strengthened by precipitation of γ' ordered phases with a stoichiometric Ni_3(Al,Ti,Nb) ratio. However, formation of MC carbides with the needle-like morphology at such specific site was unexpected during the applied heat-treatment condition. The MC carbide consists of Ti and Nb elements, which are strongly interacting with hydrogen and also contributing as the constituents of γ' precipitates. Thereby the carbide precipitation could affect HE as well as its fundamental role on the mechanical properties in IN740H superalloy. In this context, the effect of the needle-like MC carbide on HE was investigated in this study.

2. Materials and Methods

The chemical composition of IN740H superalloy used in this study is Ni-24.3Cr-19.5Co-1.40Al-1.41Ti-1.32Nb-0.62Mo-0.88Fe-0.21Mn-0.17Si-0.04Cu-0.03C-0.0033B-0.006P-0.002S in wt.%. The alloy was solution treated at 1473 K for 1 h and water-quenched (hereafter, this specimen will be referred as CG-S standing for Coarse-Grained Solution-treated). For grain refinement, some of CG-S specimen were 70% cold-rolled at room-temperature, and then solution treated at 1393 K for 10 min, followed by water-quenching (referred as FG-S hereafter, standing for Fine-Grained Solution-treated). Two solution treated specimens were subsequently aged at 1173 K for 100 h, and then cooled in air. For convenience, these aged specimens are referred as CG-A and FG-A, respectively after the CG-S and FG-S specimens, hereafter. The specimens aged at the same temperature have similar total fraction of precipitate and their size. Additionally, the grain size of the aged specimens was not significantly changed during the aging process. Detailed information on the initial microstructure was described in our previous report [20].

Morphology, distribution and constituent elements of the precipitates in initial microstructure were analyzed using a transmission electron microscope (TEM, Talos F200X, FEI, Hillsboro, OR, USA) equipped with an EDS system. The TEM foils for non-deformed specimens were prepared by twin-jet electropolishing (TenuPol-5, Struers, Ballerup, Denmark) using an electrolyte consisting of 10 % perchloric acid and 90% methanol at 243 K.

Tensile specimens with $10^{l} \times 1^{w} \times 0.3^{t}$ mm^3 dimensions at gauge portion were cut along rolling direction by electro-discharge machining. The surface of the machined tensile specimen was then mechanically polished, and the final polishing was done with a colloidal silica with a size of 0.02 μm to form mirror surface. The final thickness of the tensile specimens was about ~250 μm. The tensile specimens were thermally charged with 99.9999% pure hydrogen gas at 573 K and 15 MPa for 72 h utilizing the method described earlier [21–25], and then stored in liquid nitrogen right after hydrogen charging to minimize hydrogen release out of the specimen. It took less than 5 min for the hydrogen-charged specimens to move to the liquid nitrogen storage from the hydrogen charging cylinder. Nevertheless, all of the testing was completed within 24 h after hydrogen charging.

The hydrogen-charged specimen was taken out of the liquid nitrogen and left at room-temperature within 5 min, and then tensile testing was performed at a strain rate of 10^{-4} s^{-1} using a 300 N mini-tensile testing machine (Mtest300, Gatan Inc., Pleasanton, CA, USA). After failure, fracture surface and gauge portion near fracture surface of the specimens were observed using a field emission scanning electron microscope (FE-SEM, S-4300SE, Hitachi, Tokyo, Japan) under 20 kV with an energy dispersive X-ray spectroscopy (EDS, XFlash, Bruker, Karlsruhe, Germany).

In order to quantify the hydrogen content, thermal desorption analysis was conducted for the hydrogen-charged specimens using thermal desorption spectroscopy (TDS) with a quadruple mass spectrometer (R-DEC, Tsukuba, Japan) having a measurement accuracy of 0.01 wppm at a heating rate of 300 K/h. Hydrogen charging process and the time interval between hydrogen charging and TDS testing was set to be identical to that for the above-mentioned tensile testing condition.

3. Results and Discussion

3.1. Initial Microstructure

SEM images of FG-S and CG-S specimens are shown in Figure 1a,b, respectively. The average grain size with annealing twin boundary of solution-treated specimens was estimated to be 15 and 120 μm, respectively for FG-S and CG-S specimens. Additionally, annealing twins are well developed for both specimens [20]. Primary blocky MC carbides were randomly distributed in both specimens, as indicated by white circles in both figures. For better understanding of the initial microstructure, each initial microstructure was schematically drawn in Figure 1c,d for FG-S and CG-S, respectively. Most prominent difference between them as well as the grain size is the morphology of twin boundaries inside grains. For FG-S specimen, annealing twin boundaries are well-developed. The annealing twins crossed the grain perfectly from one side to the other, and the typical appearance of the twin boundary is called a coherent twin boundary (CTB), as pointed by the green arrows in Figure 1a,c. For CG-S specimen, however, larger portion of twin boundaries appears but their appearance looks imperfect: most of the twins do not completely cross the grain and stops along the way. Therefore, an imperfect interface formed as indicated by red arrows in Figure 1b,d. The imperfect interface is a so-called incoherent twin boundary (ITB), and the ITB has higher interfacial energy compared with the CTB [26], although both the CTB and ITB are stable, still having lower interfacial energy than typical random high-angle boundaries.

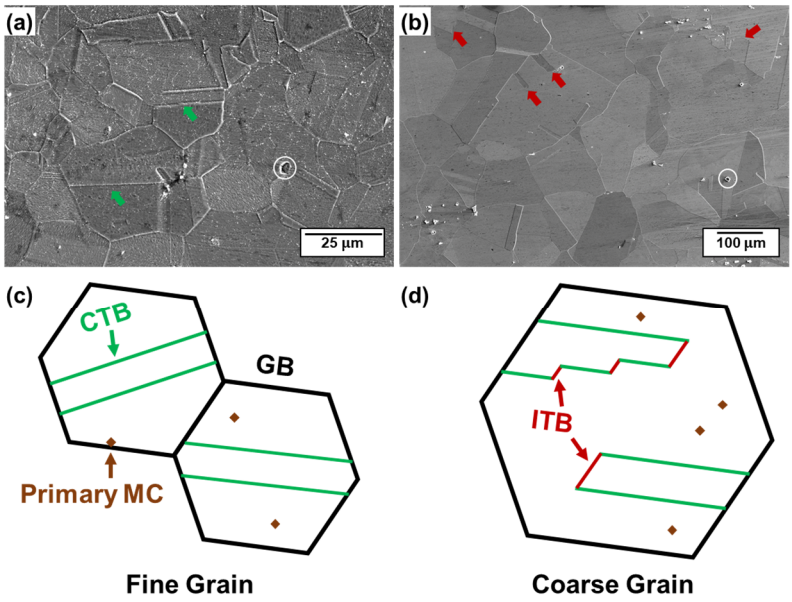

Figure 1. SEM images of (**a**) FG-S and (**b**) CG-S specimens. The green and red arrows, and white circles indicate coherent and incoherent twin boundary, and primary blocky MC carbide, respectively. Schematic images of the microstructure of (**c**) FG-S and (**d**) CG-S specimens.

Figure 2 presents SEM images of FG-A (Figure 2a) and CG-A (Figure 2b,c) specimens. It commonly shows that precipitates formed at grain boundaries in both specimens. However, precipitation behavior around TBs noticeably looks different between both specimens; as shown in Figure 2b–d, needle-like precipitates formed around ITBs. For better under-

standing of the precipitation behavior in both aged specimens, TEM-EDS images were presented in Figure 3. As shown in Figure 3a, grain boundaries and neighboring regions are decorated by coarser γ' precipitates and MC carbides while finer γ' precipitates are distributed inside grains in FG-A specimen. Although Figure 3b magnifies the region of ITB not showing grain boundary, similar tendency was observed for CG-A specimen (not shown) and the fine γ' precipitation inside grains can be observed in the left image of Figure 3b. On the other hand, needle-like carbides formed around ITBs only in case of CG-A specimen, as shown in Figure 3b. In our previous report [20], the needle-like carbides were identified as MC-type of (Ti,Nb)C carbide from selected area diffraction (SAD) pattern analysis. The longitudinal direction of the needle-like MC carbides is parallel to CTBs due to the directional stress field around ITB [27]. Since ITBs were introduced more in CG-S specimen than in FG-S specimen as shown in Figure 1b,d, needle-like MC carbide is more likely to form in CG-A specimen while secondary MC carbides with blocky shape could form at other preferential nucleation sites also in FG-A specimen.

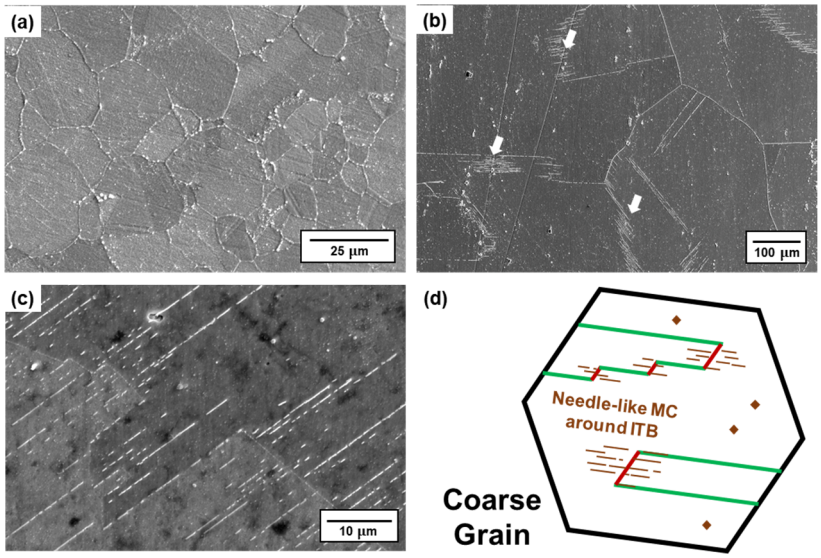

Figure 2. SEM images of (**a**) FG-A and (**b**) CG-A specimens. The white arrows indicate needle-like MC carbides around incoherent twin boundary (ITB). (**c**) The magnified image showing needle-like MC carbides in CG-A specimen. (**d**) Schematic image of the microstructure of CG-A specimen.

Meanwhile, a γ' precipitate-free zone (PFZ) was observed around twin boundary and grain boundary, as shown in Figure 3a,b. It can be attributed (i) to coarse γ' phases at grain boundary depriving the region of the γ' forming elements in both the specimens aged at 1173 K (although not shown in Figure 3b, the coarse γ' phases and PFZ around them were also observed for CG-A specimen), and (ii) to the needle-like MC carbide containing Ti and Nb, which must have depleted the γ' forming elements, around twin boundary in the CG-A specimen as shown in Figure 3b.

3.2. Tensile Property with and without Hydrogen

Figure 4a,b show engineering stress–strain curves with and without hydrogen charging for the solution-treated specimens and the aged specimens. FG and CG specimens were indicated by red and blue lines, respectively, while non-charged and hydrogen-charged specimens were drawn by solid and dashed lines, respectively. The typical grain size effect was observed that yield stress and ultimate tensile strength (UTS) increased, and uniform elongation slightly decreased with decreasing grain size in both -S and -A specimens.

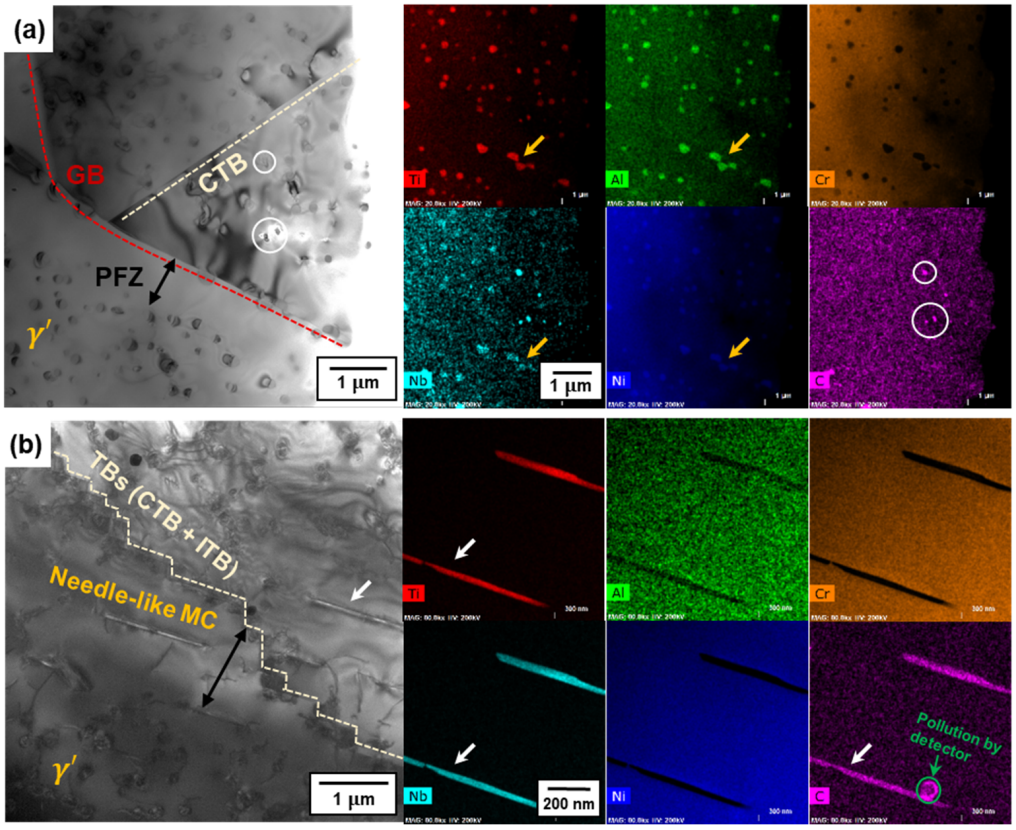

Figure 3. TEM-EDS images of (**a**) FG-A and (**b**) CG-A specimens. The white circles and yellow arrows in (**a**) indicate primary carbides and coarse gamma-prime precipitates at grain boundaries and the neighboring region, respectively. The white arrows in (**b**) indicate needle-like MC carbide around incoherent twin boundary.

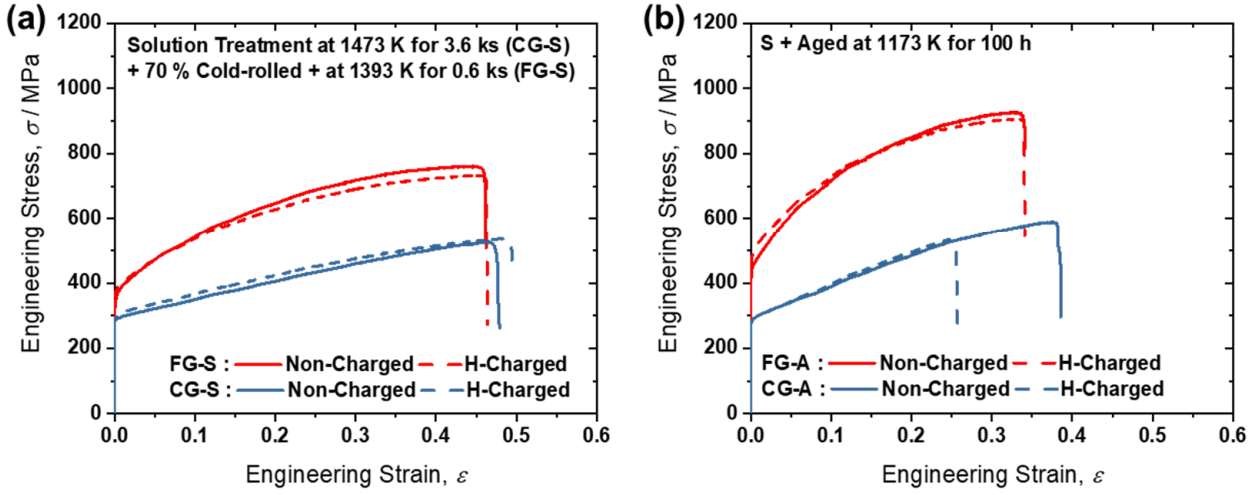

Figure 4. (**a**) Engineering stress–strain curves of (**a**) solution-treated (-S) and (**b**) aged (-A) specimens. The red and blue lines indicate FG- and CG- specimens, respectively. The solid and dotted lines mean the non-charged and the hydrogen-charged specimens, respectively.

After the aging process, yield stress and UTS increased but elongation decreased, and the strengthening effect by the aging process is more prominent in FG-A specimen than CG-A specimen. As shown in Figure 3, γ' precipitate as well as grain size could strengthen Ni-based superalloys [10–14]. Nevertheless, yield stress of both -A specimens are quite lower than most γ' precipitate-hardened superalloys [10–12] since the adopted aging temperature in this study is much higher and thereby could make -A specimens over-aged. Formation

of needle-like MC carbides in CG-A specimen significantly restricts γ' precipitation around twin boundaries since two precipitates consist of Ti and Nb elements, and the strengthening by the MC carbides seems to be less effective than that by γ' precipitates.

After hydrogen charging, only elongation of CG-A specimens noticeably decreased while the other specimens appeared unaffected, as shown in the dashed lines in Figure 4a,b. Total elongation of specimens with and without hydrogen was indicated in Table 1. The ductility loss of those specimens was calculated by the following Equation (1).

$$\text{Ductility loss (\%)} = \{(\text{El.}_\text{N} - \text{El.}_\text{H})/\text{El.}_\text{N}\} \times 100 \quad (1)$$

where El._N is the elongation for non-charged specimen and El._H the elongation for hydrogen-charged specimen. The ductility loss was estimated to be 32% for the CG-A specimen while the other specimens did not show any degradation by the absorbed hydrogen.

Table 1. Elongation with and without hydrogen charging, and ductility loss.

Specimen	without H (El._N)	with H (El._H)	Ductility Loss (%)	Specimen	without H (El._N)	with H (El._H)	Ductility Loss (%)
FG-S	0.46	0.46	0	CG-S	0.48	0.49	−0.02
FG-A	0.34	0.34	0	CG-A	0.38	0.26	0.32

3.3. Fracture Behavior

Fractography results were presented in Figure 5 for overall fracture surface and in Figure 6 for the magnified image of the aged specimens (FG- and CG-A) with or without hydrogen charging. At first, in case of FG-A specimen, larger sizes of dimples around smaller typical dimples were frequently shown in non-charged FG-A specimen, as pointed by the yellow arrows in Figure 6a. At the inner region of the dimples, relatively larger or smaller size of precipitates were observed. As compared with the microstructure of the FG-A specimen Figures 2a and 3a, the precipitates can be inferred as a blocky primary MC carbide for the larger ones, and a secondary MC carbide or coarsened γ' precipitates formed during aging process for the smaller ones. Therefore, it is understood that micro-voids primarily occur around the precipitates, followed by micro-voids coalescence (MVC) process in the FG-A specimens. Additionally, the γ' precipitates in grain interior seem not to be influential for fracture behavior. This MVC process with ductile fracture was maintained even after hydrogen charging in FG-A specimens, as shown in Figures 5b and 6b. This ductile fracture behavior was also commonly observed (although not shown in the paper) in both solution-treated FG-S and CG-S specimens without degradation of ductility by hydrogen charging.

In the case of non-charged CG-A specimen, MVC process with some occasional shear fracture related to coarse grain size was dominant fracture mode as shown in Figure 5c. In particular, elongated dimples looking like a long and deep valley were presented in the magnified fracture surface (the white arrows in Figure 6c). These elongated dimples are likely to come from the twin boundaries, which was decorated by needle-like MC carbides, as shown in Figure 2b–d. After hydrogen charging, however, fracture behavior strikingly changed when the fracture mode transited from the MVC process to intergranular fracture, as shown in Figure 5d. In the magnified fracture surface (Figure 6d), it is noteworthy that the elongated dimples appear adjoining with the interface between intergranular fracture surfaces (the dotted white lines).

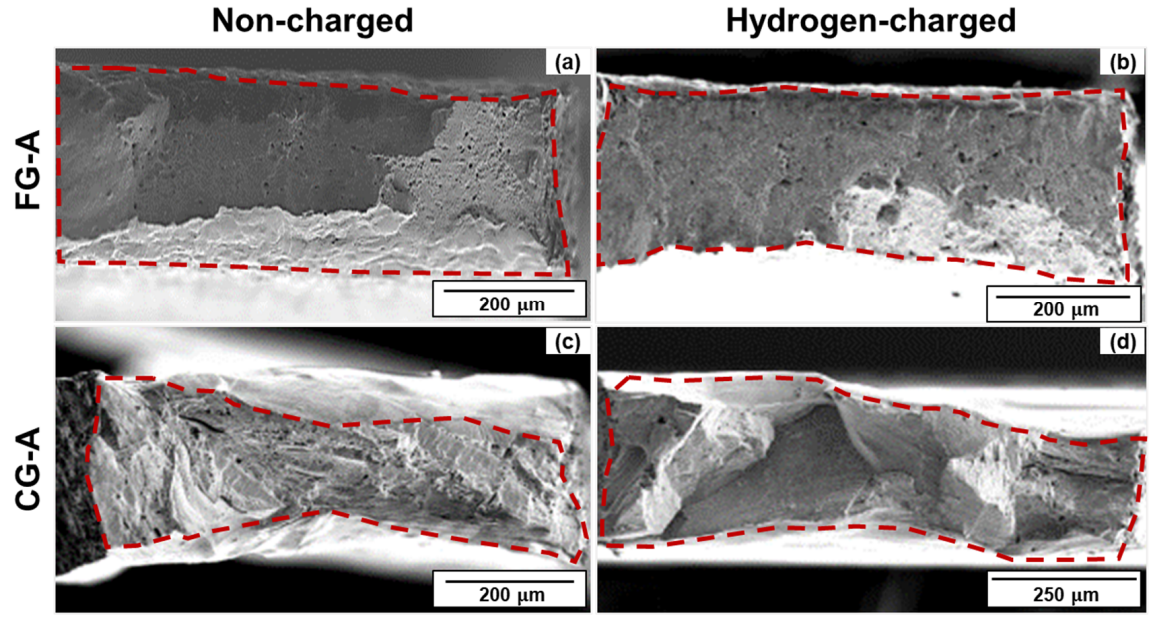

Figure 5. Fractographs of (**a**,**b**) FG-A and (**c**,**d**) CG-A specimens; in (**a**,**c**) non-charged and (**b**,**d**) hydrogen-charged conditions. The red dotted line in each image indicates boundary of fracture surface.

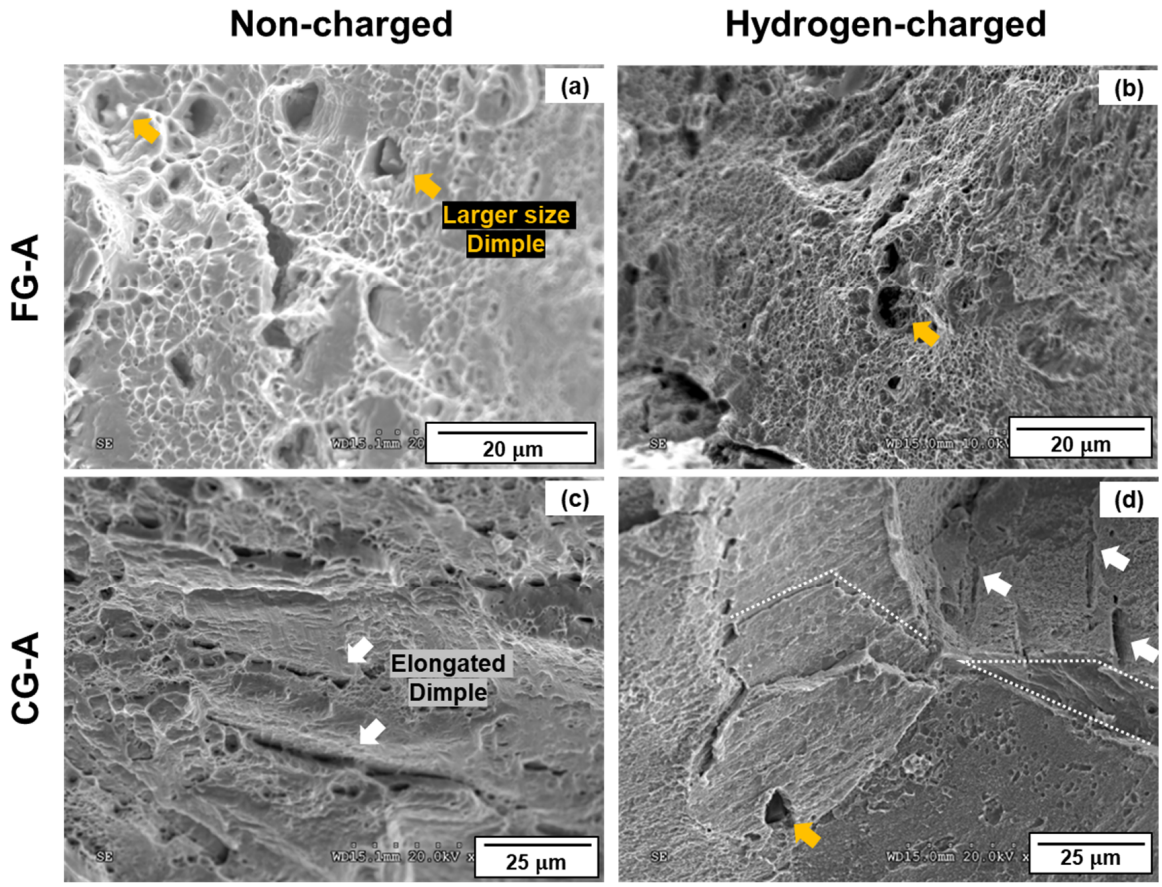

Figure 6. The magnified image (**a**–**d**) of each fractograph shown in Figure 5. The yellow arrows indicate dimples of larger size originating from primary block MC carbides, on the other hand, the white arrows show elongated dimples that appeared only in CG-A specimens.

4. Discussion

4.1. Hydrogen Trapping Behavior

The experimental TDS curves of the specimens used in this study were shown by the black line in Figure 7a–d. It would be difficult to figure out if a thermal decomposition behavior is composed of a single peak or multiple peaks because even a single peak decomposition could have an asymmetric shape [28]. However, in this work, we made an assumption that the observed thermal decomposition could be decomposed into two peaks by referencing the other works on similar materials [29,30] to make a discussion regarding what type of microstructural feature could be dominantly influencing the hydrogen absorption behavior. Using a multiple peak analyzer (built-in Origin 2022 software), non-linear curve fitting based on a Gaussian model was performed to decompose the apparent single peak of each experimental TDS curve into two peaks; the lower temperature peak (red line) and the higher temperature peak (green line) in each TDS curve (Figure 7), and the cumulative fit curve (blue line) of both peaks are matched well with the experimental TDS data (black line). The peak temperatures of the curves are indicated in Table 2. It should be noted here that the decomposition of the TDS peak is intended not to carry out a rigorous analysis but to acquire a rough idea on which type of trapping site is more dominantly affected by annealing treatment.

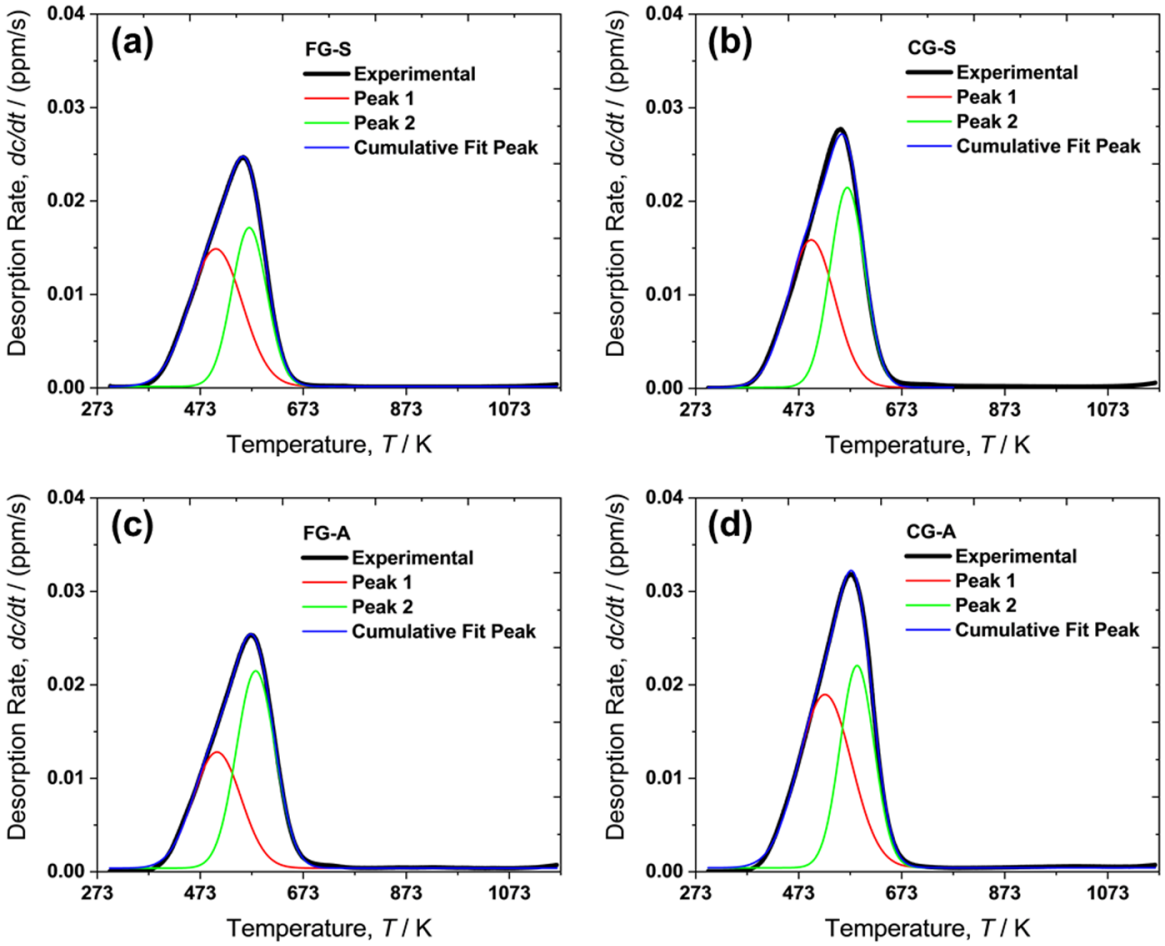

Figure 7. Hydrogen desorption curve of (**a**) FG-S, (**b**) CG-S, (**c**) FG-A, and (**d**) CG-A specimens. The cumulative curve (blue) of the sum of two fitted curves (red and green) match well with the experimental TDS curve (black) in each specimen.

Table 2. Peak temperature and the absorbed hydrogen content acquired by experimental and fitted TDS curves.

	Fitted Curves				Experimental Curve	
	Peak 1		Peak 2			
Specimen	**Peak Temperature (K)**	**Hydrogen Content, C_1 (wppm)**	**Peak Temperature (K)**	**Hydrogen Content, C_2 (wppm)**	**Peak Temperature (K)**	**Total Hydrogen Content (wppm)**
FG-S	503	19.7	568	22.1	555	41.8
CG-S	496	19.3	567	26.2	552	45.5
FG-A	505	15.5	580	30.0	571	45.5
CG-A	524	26.3	587	28.9	573	55.2

The lower and higher temperature peaks for the -S specimens occur at ~500 and ~570 K, respectively, and both peak temperatures certainly increased by aging treatment. The degree of the increment in the peak temperatures by aging treatment was higher in CG specimens. Considering that the TDS measurement was done with constant thickness of specimens, ~250 μm, the observed shift in peak temperature could be attributed to the decrease in effective hydrogen diffusivity after aging treatment which could take place by the increase in hydrogen trapping site. Both peak temperatures of -A specimens matched well with other precipitation-hardening superalloys, IN718, IN725, and Monel K-500 [29,30]. According to the previous studies [30], the lower temperature peak is related to the sum of the hydrogen in lattice interstitial sites and the lattice hydrogen with low-energy reversible trap sites, such as dislocations, twin boundaries, and low-energy boundaries, whereas the higher temperature peak are likely the stronger reversible trap sites, such as grain boundaries, γ', and γ''.

The hydrogen content of two fit curves in each specimen as well as the total hydrogen content (up to 723 K) were summarized in Table 2. The hydrogen content in each curve was calculated by integrating the curve. Hereafter, the hydrogen contents for the lower and higher temperature fit curves are referred to as C_1 and C_2, respectively. C_1 and C_2 for -S specimens were calculated to be 19.7 and 22.1 wppm for FG-S specimen, and 19.3 and 26.2 wppm for CG-S specimen, respectively. Similar content of C_1 in both -S specimens are likely due to the comparable annealing twin boundary fraction between both -S specimens [20] as well as the same hydrogen charging condition rendering the same lattice hydrogen concentration based on a Sieverts' law relationship. On the other hand, C_2 in CG-S specimen was higher than that in FG-S specimen which indicates that the annealing treatment at higher temperature (CG-S) resulted in higher amount of trapping sites with stronger bonding energy. This difference is not fully understood because the CG-S specimen has less grain boundary area than FG-S and the detailed mechanism should be further investigated. Meanwhile, primary blocky MC carbides are generally regarded as the irreversible hydrogen trapping site [29,31], and thus the peak concerning the carbides should have appeared at higher temperature than the peaks of two fit curves if the carbides acted as effective hydrogen trapping site. However, other peaks were not clearly observed above 723 K, and also the hydrogen content above 723 K of all specimens was measured to be less than 1 wppm. Therefore, it can be seen that primary block MC carbides are not considered as the effective hydrogen trapping site regardless of grain size variation in this study primarily due to the low number density.

On the other hand, aging treatment accompanying precipitation seemed to change hydrogen trapping behavior between both -A specimens. The total hydrogen content of both -A specimens increased by the aging treatment; from 41.8 to 45.5 wppm for FG specimen and from 45.5 to 55.2 wppm for CG specimen. As compared to C_1 and C_2 of -S specimens, C_2 prominently increased while C_1 decreased for FG-A specimen. This means that the interface between matrix and γ' effectively trapped hydrogen atoms contributing

to the increment in C_2 in FG-A specimen, as reported in the previous studies [3,29,30]. As opposed to the FG-A specimen, however, C_1 significantly increased and C_2 marginally increased despite the precipitation of γ' as well in the CG-A specimen. The difference between both -A specimens is that a large amount of needle-like MC carbides with its surrounding PFZ formed near the twin boundaries in the CG-A specimen, as shown in Figures 2b and 3b. Therefore, it is reasonable to infer that hydrogen atoms in CG-A specimen are more trapped around twin boundaries decorated with the needle-like MC carbides and likely at the interface between the matrix and the needle-like MC carbide. The needle-like MC carbides are nucleated at stacking faults at or near incoherent twin boundaries [20], and thus the interface between matrix and the carbide (especially the interface parallel to the longitudinal direction) might maintain good coherency. Unlike the interface between matrix and the primary blocky MC carbide that are generally regarded as an incoherent interface with a strong irreversible trapping site, the interface between matrix and the needle-like MC carbide are considered as relatively weak hydrogen trapping site. It is reported that TDS peak temperature and hydrogen trap binding energy of carbide are dependent on interfacial coherency with matrix [32,33].

Looking at the experimental TDS data, the annealing treatment on CG specimen increased the hydrogen absorption from 45.5 to 55.2 (difference is 9.7) wppm while the annealing on the FG specimen showed only minor increase, from 41.8 to 45.5 (difference is 3.7) wppm. With the help of peak decomposition analysis, it could be concluded that the annealing treatment and resultant formation of γ' contributed to the increase in hydrogen absorption to some extent (for example, 3.7 wppm for FG specimen) while the formation of needle-like MC carbide also contributed with comparable or even higher amount that the 9.7 wppm increase in CG specimen is attributed to the cooperative contribution of both γ' and needle-like MC carbide.

4.2. Hydrogen-Induced Intergranular Fracture

In both hydrogen-charged -S specimens, hydrogen-induced degradation related to mechanical properties was not detected as shown in Figure 4. This means a critical hydrogen concentration needed to induce intergranular fracture was not attained in both -S specimens although large amounts of hydrogen were trapped at grain boundaries, as shown in Table 2. For both -A specimens, on the other hand, ductility significantly decreased only in hydrogen-charged CG-A specimen although γ' precipitates were commonly formed. It shows that for the decrease in ductility of the CG-A specimen, the synergistic effect of hydrogen and needle-like MC carbide on deformation behavior around ITB is more of the main factor than slip planarity by γ' shearing.

Figure 8a,b show the SEM images indicating the deformation characteristic of the needle-like MC carbides around ITBs in non-charged CG-A specimen at the fracture strain. The SEM images were taken at the region near fractured surfaces. It is clearly shown that the needle-like carbides in the non-charged specimen were obviously tolerant to higher fracture strain of about 0.38 showing significant strain accumulation without any defects (Figure 8a,b). There are two important factors influencing on deformation behavior of neighboring twin boundaries in the CG-A specimen: (i) needle-like MC carbide, and (ii) its surrounding PFZ. Generally, carbides are relatively stronger than matrix in metallic materials, and the carbide/matrix interface are regarded as the main source of formation of micro-voids, through decohesion of the interface and/or fracture of the carbides by dislocation pile-up during deformation. Accordingly, larger size of dimples originated from carbides are shown in fracture surface, as the evidence of active MVC process near the carbide/matrix interface, as shown in Figure 6. However, the size of elongated dimples (white arrows in Figure 6c,d) formed by needle-like MC carbides looks comparable with its neighboring dimples. This is closely related to the fact that the needle-like carbide/matrix interface sufficiently accumulated the strain in the surrounding area, as shown in Figure 8a,b, nearly up to the fracture strain. The sufficient strain accumulation near the interface is linked to the presence of PFZ in the vicinity of the needle-like carbides. PFZ is a

relatively softer region since the precipitates adjacent to the PFZ deprive its constituent elements. PFZ could rather accompany deformation [34], and also it restrains crack extension as a role of relieving stress concentration [35]. From this point of view, it can be said that the presence of PFZ effectively restricts the formation of micro-voids at the needle-like MC carbide/matrix interface, and thus sufficient strain accumulation at the interface decreases the sensitivity to intergranular fracture along twin boundaries, although lots of carbides were decorated near twin boundaries in non-charged CG-A specimen.

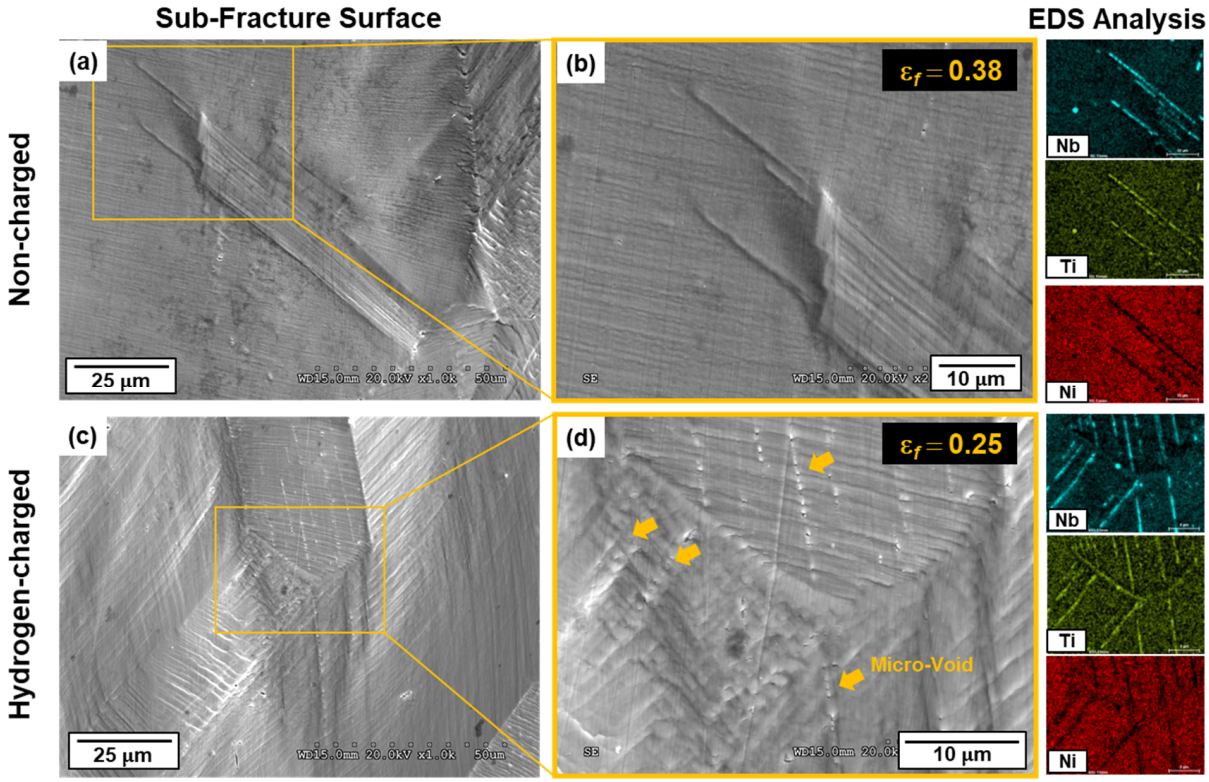

Figure 8. SEM images of the surface area near the fracture surface of (**a**,**b**) the non-charged and (**c**,**d**) the hydrogen-charged CG-A specimens, showing incoherent twin boundary and needle-like MC carbide. EDS maps of Nb, Ti, and Ni indicate the position of the needle-like MC carbides in (**b**,**d**). The yellow arrows in (**d**) indicate the micro-voids at the carbide/matrix interface.

On the other hand, the inherent localized deformation behavior around twin boundaries in CG-A specimen seems to behave differently when exposed to hydrogen. Figure 8c,d show that needle-like MC carbides looked separated and thereby micro-voids formed even at lower fracture strain of about 0.25. It is clear that hydrogen uptake accelerated void formation at or near the carbide/matrix interface at earlier strain. As shown in Figure 7 and Table 2, a lot of hydrogen atoms in CG-A specimen were trapped around the needle-like MC carbide/matrix interface as well as twin boundaries regarding those sites as a reversible weak hydrogen trapping site. When hydrogen is present at such second phase/matrix interface, the formation of micro-voids/cracks along the interface can occur readily in the framework of hydrogen-enhanced decohesion (HEDE) model [36]. Moreover, dislocation pile-up process could be accelerated at the interface due to the presence of PFZ implying that hydrogen enhances a slip localization in PFZ as operating hydrogen-enhanced localized plasticity (HELP) model [37]. Additionally, hydrogen atoms can be paired with moving dislocations, and the hydrogen-decorated dislocations are more piled-up at the interface [38]. As a result, the enhanced dislocation pile-up process and hydrogen accumulation at the interface accelerate the formation of micro-voids/cracks at needle-like MC carbide/matrix interface at earlier strain.

Accordingly, the complex interaction between hydrogen and the needle-like carbide matrix interface as well as PFZ would render a large number of micro-void/crack to be densely distributed near twin boundaries during deformation. This would impose much higher stress on its neighboring twin boundaries and/or grain boundaries because of the reduction in the effective area capable of sustaining the applied load. Furthermore, strain is readily accumulated to the boundaries since the carbide/matrix interface can no longer absorb strain and the boundaries themselves interact with the trapped hydrogen atoms. As a result, the local stress concentration at the boundaries reaches the critical value for intergranular crack initiation leading to the prevailed intergranular fracture surface.

In summary, most previous studies on hydrogen embrittlement of several Ni-based superalloys have focused on localized deformation enhanced by shearing of γ' or γ'' precipitates [10–14]. However, this study clearly shows that, in a case that inevitable phase of carbides in superalloys form at a specific site with distinct morphology in their microstructure, the carbides could also affect hydrogen embrittlement of the materials. For the usage of Ni-based superalloys under the possibility of hydrogen penetration, therefore, control of morphology and nucleation site of carbides would be a critical requirement that should be considered.

5. Conclusions

In this study, the effect needle-like MC carbides around ITBs have on the HE of IN740H Ni-based superalloy was investigated, and the obtained conclusions are as follows:

1. For the FG-S specimen, the annealing twin boundaries developed well as the typical appearance of CTB. For the CG-S specimen, however, a larger portion of twin boundaries appeared, but their appearance was imperfect: most of the twin boundaries did not completely cross the grain and stopped along the way, which led to a large portion of ITB in the microstructure. After the aging process, needle-like MC carbides formed around ITBs only in the CG-A specimen.
2. After hydrogen charging, only the elongation of CG-A specimens noticeably decreased: The ductility loss was estimated to be 32% for the CG-A specimen, while the other specimens did not decrease. In the fractography result, the fracture behavior strikingly changed in the CG-A specimen by hydrogen absorption: the fracture mode transits from the MVC process to intergranular fracture. Additionally, elongated dimples appeared, adjoining with the interface between intergranular fracture surfaces.
3. TDS curves indicated that annealing with the coarse-grained condition (CG-A) resulted in the highest amount of hydrogen absorption, implying that the only characteristic difference of the CG-A, needle-like MC carbide, could be the dominant factor increasing the hydrogen absorption. Additionally, decomposition of the experimentally obtained TDS curves based on the assumption of two different trapping sites having Gaussian distribution showed that the peak area of the lower trapping energy (C_1) increased more than that for higher trapping energy (C_2) for CG-A compared to CG-S, which suggests that the interface between the needle-like MC carbide and the matrix could work as a weak hydrogen trapping site.
4. In the presence of hydrogen in the CG-A specimen, deformation was more localized around ITBs and dislocations were promptly piled-up at the interface between the needle-like MC carbide and the matrix. This accelerated micro-void/crack formation and coalescence process at the interface. It imposed much higher load on the neighboring region, and finally led to hydrogen-induced intergranular fracture at ITBs at earlier strain.

Author Contributions: Conceptualization & methodology, S.-Y.L.; formal analysis & investigation, S.-Y.L., H.-J.K. and C.-H.A.; writing—original draft preparation, S.-Y.L.; writing—review and editing, J.-Y.S.; supervision, S.-W.B., J.-H.S. and J.-Y.S.; project administration, J.-H.S. and J.-Y.S.; funding acquisition, J.-Y.S. All authors have read and agreed to the published version of the manuscript.

Funding: This work was supported by the Korea Institute of Science and Technology (KIST) [grant number 2E31851].

Data Availability Statement: Not applicable.

Conflicts of Interest: The authors declare no conflict of interest.

References

1. Tarzimoghadam, Z.; Rohwerder, M.; Merzlikin, S.V.; Bashir, A.; Yedra, L.; Eswara, S.; Ponge, D.; Raabe, D. Multi-scale and spatially resolved hydrogen mapping in a Ni–Nb model alloy reveals the role of the δ phase in hydrogen embrittlement of alloy 718. *Acta Mater.* **2016**, *109*, 69–81. [CrossRef]
2. Tarzimoghadam, Z.; Ponge, D.; Klöwer, J.; Raabe, D. Hydrogen-assisted failure in Ni-based superalloy 718 studied under in situ hydrogen charging: The role of localized deformation in crack propagation. *Acta Mater.* **2017**, *128*, 365–374. [CrossRef]
3. Xiong, J.; Zhu, Y.; Li, Z.; Huang, M. Hydrogen-enhanced interfacial damage in Ni-based single crystal superalloy. *Scr. Mater.* **2018**, *143*, 30–34. [CrossRef]
4. Zhang, Z.; Obasi, G.; Morana, R.; Preuss, M. Hydrogen assisted crack initiation and propagation in a nickel-based superalloy. *Acta Mater.* **2016**, *113*, 272–283. [CrossRef]
5. Rezende, M.C.; Araujo, L.S.; Gabriel, S.B.; dos Santos, D.S.; de Almeida, L.H. Hydrogen embrittlement in nickel-based superalloy 718: Relationship between $\gamma' + \gamma''$ precipitation and the fracture mode. *Int. J. Hydrog. Energy* **2015**, *40*, 17075–17083. [CrossRef]
6. Seita, M.; Hanson, H.P.; Gradecak, S.; Demkowicz, M.J. The dual role of coherent twin boundaries in hydrogen embrittlement. *Nat. Commun.* **2015**, *6*, 6164. [CrossRef] [PubMed]
7. Bang, H.R.; Park, J.; Seong, H.G.; Kim, S.J. Effect of Minor Alloying Elements (C, Ni, Cr, Mo) on the Long-Term Corrosion Behaviors of Ultrahigh-Strength Automotive Steel Sheet in Neutral Aqueous Environment. *Korean J. Met. Mater.* **2022**, *60*, 35–45. [CrossRef]
8. Hwang, A.I.; Lee, D.G.; Jung, Y.; Koo, J.M.; Cho, J.D.; Lee, J.S.; Suh, D.W. Influence of Microstructure Constituents on the Hydrogen-Induced Mechanical Degradation in Ultra-High Strength Sheet Steels. *Met. Mater. Int.* **2021**, *27*, 3959–3967. [CrossRef]
9. Kobayashi, N.; Koyama, M.; Kobayashi, K.; Hojo, T.; Akiyama, E. Hydrogen Embrittlement Behavior of Pure Ni and Ni–20Cr Alloy with Different Grain Sizes. *Mater. Trans.* **2022**, *63*, 247–256. [CrossRef]
10. Harte, A.; Atkinson, M.; Smith, A.; Drouven, C.; Zaefferer, S.; da Fonseca, J.Q.; Preuss, M. The effect of solid solution and gamma prime on the deformation modes in Ni-based superalloys. *Acta Mater.* **2020**, *194*, 257–275. [CrossRef]
11. Maciejewski, K.; Ghonem, H. Isotropic and kinematic hardening as functions of gamma prime precipitates in a nickel-based superalloy. *Int. J. Fatigue* **2014**, *68*, 123–135. [CrossRef]
12. Goodfellow, A.J. Strengthening mechanisms in polycrystalline nickel-based superalloys. *Mater. Sci. Tech.* **2018**, *34*, 1793–1808. [CrossRef]
13. Sinha, N.K. Short strain relaxation/recovery tests for evaluating creep response of nickel-base superalloys like IN-738LC. *J. Mater. Sci. Lett.* **2001**, *20*, 951–953. [CrossRef]
14. Shenoy, M.; Tjiptowidjojo, M.; McDowell, D. Microstructure-sensitive modeling of polycrystalline IN 100. *Int. J. Plast.* **2008**, *24*, 1694–1730. [CrossRef]
15. Araujo, L.S.; Guimaraes, A.V.; Siqueira, M.C.; Mendes, M.C.; Mallet, L.; dos Santos, D.S.; de Almeida, L.H. The influence of the processing route on the fragmentation of (Nb,Ti)C stringers and its role on mechanical properties and hydrogen embrittlement of nickel based alloy 718. *Int. J. Hydrog. Energy* **2021**, *46*, 16164–16178. [CrossRef]
16. Young, G.A.; Scully, J.R. Evidence that carbide precipitation produces hydrogen traps in Ni-17Cr-8Fe alloys. *Scr. Mater.* **1997**, *36*, 713–719. [CrossRef]
17. Symons, D.M. The effect of carbide precipitation on the hydrogen-enhanced fracture behavior of alloy 690. *Metall. Mater. Trans. A* **1998**, *29A*, 1265–1277. [CrossRef]
18. Lee, J.; Lee, T.; Kwon, Y.J.; Mun, D.J.; Yoo, J.Y.; Lee, C.S. Effects of vanadium carbides on hydrogen embrittlement of tempered martensitic steel. *Met. Mater. Int.* **2016**, *22*, 364–372. [CrossRef]
19. Depover, T.; Verbeken, K. The detrimental effect of hydrogen at dislocations on the hydrogen embrittlement susceptibility of Fe-C-X alloys: An experimental proof of the HELP mechanism. *Int. J. Hydrog. Energy* **2018**, *43*, 3050–3061. [CrossRef]
20. Lee, S.Y.; Kim, B.K.; Lee, S.H.; Kim, D.I.; Shim, J.H.; Jung, W.S.; Suh, J.Y. Formation of needle-like MC carbide at or near incoherent twin boundary in IN740H Ni-based superalloy. *J. Alloy. Compd.* **2020**, *813*, 152222. [CrossRef]
21. Lee, J.; Park, H.; Kim, M.; Kim, H.J.; Suh, J.Y.; Kang, N. Role of Hydrogen and Temperature in Hydrogen Embrittlement of Equimolar CoCrFeMnNi High-entropy Alloy. *Met. Mater. Int.* **2021**, *27*, 166–174. [CrossRef]
22. Kim, H.J.; Cho, M.K.; Kim, G.; Lee, S.Y.; Jo, M.G.; Kim, H.; Suh, J.Y.; Lee, J. Influence of Hydrogen Absorption on Stacking Fault of Energy of a Face-Centered Cubic High Entropy Alloy. *Met. Mater. Int.* **2022**, *28*, 2637–2645. [CrossRef]
23. Zhao, Y.; Lee, D.H.; Seok, M.Y.; Lee, J.A.; Phaniraj, M.P.; Suh, J.Y.; Ha, H.Y.; Kim, J.Y.; Ramamurty, U.; Jang, J.I. Resistance of CoCrFeMnNi high-entropy alloy to gaseous hydrogen embrittlement. *Scr. Mater.* **2017**, *135*, 54–58. [CrossRef]
24. Phaniraj, M.P.; Kim, H.J.; Suh, J.Y.; Shim, J.H.; Park, S.J.; Lee, T.H. Hydrogen embrittlement in high interstitial alloyed 18Cr10Mn austenitic stainless steels. *Int. J. Hydrog. Energy* **2015**, *40*, 13635–13642. [CrossRef]

25. Kim, H.J.; Phaniraj, M.P.; Kim, J.H.; Lee, Y.S.; Kim, D.I.; Suh, J.Y.; Lee, J.; Shim, J.H.; Park, S.J. Effect of thermal charging of hydrogen on the microstructure of metastable austenitic stainless steel. *Steel Res. Int.* **2017**, *88*, 1600063. [CrossRef]
26. Brown, J.A.; Ghoniem, N.M. Structure and motion of junctions between coherent and incoherent twin boundaries in copper. *Acta Mater.* **2009**, *57*, 4454–4462. [CrossRef]
27. Romero, R.J.; Murr, L.E. Torque-related lamellar carbide growth associated with annealing twins in 304 stainless steel. *Acta Metall. Mater.* **1995**, *43*, 461–469. [CrossRef]
28. Zaika, Y.V.; Kostikova, E.K.; Nechaev, Y.S. Peaks of Hydrogen Thermal Desorption: Simulation and Interpretation. *Tech. Phys.* **2021**, *66*, 210–220. [CrossRef]
29. Lu, X.; Ma, Y.; Wang, D. On the hydrogen embrittlement behavior of nickel-based alloys: Alloys 718 and 725. *Mater. Sci. Eng. A* **2020**, *792*, 139785. [CrossRef]
30. Ai, J.H.; Ha, H.M.; Gangloff, R.P.; Scully, J.R. Hydrogen diffusion and trapping in a precipitation-hardened nickel–copper–aluminum alloy Monel K-500 (UNS N05500). *Acta Mater.* **2013**, *61*, 3186–3199. [CrossRef]
31. Liu, L.; Zhai, C.; Lu, C.; Ding, W.; Hirose, A.; Kobayashi, K.F. Study of the effect of δ phase on hydrogen embrittlement of Inconel 718 by notch tensile tests. *Corros. Sci.* **2005**, *47*, 355–367. [CrossRef]
32. Wei, F.G.; Hara, T.; Tsuzaki, K. Precise determination of the activation energy for desorption of hydrogen in two Ti-added steels by a single thermal-desorption spectrum. *Metall. Mater. Trans. B* **2004**, *35*, 587–597. [CrossRef]
33. Wei, F.G.; Tsuzaki, K. Quantitative analysis on hydrogen trapping of TiC particles in steel. *Metall. Mater. Trans. A* **2006**, *37*, 331–353. [CrossRef]
34. Krol, T.; Baither, D.; Nembach, E. The formation of precipitate free zones along grain boundaries in a superalloy and the ensuing effects on its plastic deformation. *Acta Mater.* **2004**, *52*, 2095–2108. [CrossRef]
35. Wang, C.; Li, R. Effect of double aging treatment on structure in Inconel 718 alloy. *J. Mater. Sci.* **2004**, *39*, 2593–2595. [CrossRef]
36. Troiano, A.R. The role of hydrogen and other interstitials in the mechanical behavior of metals. *Trans. Am. Soc. Met.* **1960**, *52*, 54–80. [CrossRef]
37. Beachem, C.D. A new model for hydrogen-assisted cracking (hydrogen "embrittlement"). *Metall. Trans. A* **1972**, *3A*, 437–451. [CrossRef]
38. Guedes, D.; Malheiros, L.C.; Oudriss, A.; Cohendoz, S.; Bouhattate, J.; Creus, J.; Thebault, F.; Piette, M.; Feaugas, X. The role of plasticity and hydrogen flux in the fracture of a tempered martensitic steel: A new design of mechanical test until fracture to separate the influence of mobile from deeply trapped hydrogen. *Acta Mater.* **2020**, *186*, 133–148. [CrossRef]